Generalization of the Lyot filter and its application to snapshot spectral imaging

Alistair Gorman[1], David William Fletcher-Holmes[2] and Andrew Robert Harvey*[1]

[1]*School of Engineering and Physical Sciences, Heriot-Watt University, Edinburgh, EH144AS, UK*
[2]*Now at Cambridge Research & Instrumentation, Woburn, MA 01801, USA*
**a.r.harvey@hw.ac.uk*

Abstract: A snapshot multi-spectral imaging technique is described which employs multiple cascaded birefringent interferometers to simultaneously spectrally filter and demultiplex multiple spectral images onto a single detector array. Spectral images are recorded directly without the need for inversion and without rejection of light and so the technique offers the potential for high signal-to-noise ratio. An example of an eight-band multi-spectral movie sequence is presented; we believe this is the first such demonstration of a technique able to record multi-spectral movie sequences without the need for computer reconstruction.

OCIS codes: (110.4190) Imaging systems; (110.4234) Multispectral and hyperspectral imaging; (120.6200) Spectrometers and spectroscopic instrumentation

References and links

1. A. R. Harvey, J. E. Beale, A. H. Greenaway, T. J. Hanlon, and J. W. Williams, "Technology options for hyperspectral imaging," Proc. SPIE **4132**, 13–24 (2000).
2. L. L. Thompson, "Remote sensing using solid-state array technology," Photogramm. Eng. **45**, 47–55 (1979).
3. J. Y. Hardeberg, F. Schmitt, and H. Brettel, "Multispectral color image capture using a liquid crystal tunable filter," Opt. Eng. **41**(10), 2532–2548 (2002).
4. A. R. Harvey, and D. W. Fletcher-Holmes, "Birefringent Fourier-transform imaging spectrometer," Opt. Express **12**(22), 5368–5374 (2004).
5. T. Zimmermann, J. Rietdorf, and R. Pepperkok, "Spectral imaging and its applications in live cell microscopy," EBS Letters **546**, 87–93 (2003).
6. M. Rast, and J. L. Bezy, "The ESA Medium Resolution Imaging Spectrometer MERIS a review of the instrument and its mission," Int. J. Remote Sens. **20**(9), 1681–1702 (1999).
7. Y. R. Chen, K. Chao, and M. S. Kim, "Machine vision technology for agricultural applications," Comput. Electron. Agric. **36**(2-3), 173–191 (2002).
8. D. L. Farkas, and D. Becker, "Applications of spectral imaging: detection and analysis of human melanoma and its precursors," Pigment Cell Res. **14**(1), 2–8 (2001).
9. J. Hunicz, and D. Piernikarski, "Investigation of combustion in a gasoline engine using spectrophotometric methods", Optoelectronic and Electronic Sensors IV Proc. SPIE **4516**, 307–314 (2001).
10. P. Kauranen, S. Andersson-Engels, and S. Svanberg, "Spatial mapping of flame radical emission using a spectroscopic multi-colour imaging system," Appl. Phys. B-Photo. **53**(Issue 4), 260–264 (1991).
11. I. Alabboud, G. Muyo, A. Gorman, D. Mordant, A. McNaught, C. Petres, Y. R. Petillot, and A. R. Harvey, "New spectral imaging techniques for blood oximetry in the retina", Proc. SPIE **6631**, 6631–0L-1–10 (2007).
12. K. Gono, T. Obi, M. Yamaguchi, N. Ohyama, H. Machida, Y. Sano, S. Yoshida, Y. Hamamoto, and T. Endo, "Appearance of enhanced tissue features in narrow-band endoscopic imaging," J. Biomed. Opt. **9**(3), 568–577 (2004).
13. J. Karlholm, and I. Renhorn, "Wavelength band selection method for multispectral target detection," Appl. Opt. **41**(32), 6786–6795 (2002).
14. L. Weitzel, A. Krabbe, H. Kroker, N. Thatte, L. E. Tacconi-Garman, M. Cameron, R. Genzel, L. E. Tacconi Garman, "3D: The next generation near-infrared imaging spectrometer," Astron. Astrophys. Suppl. Ser. **119**(3), 531–546 (1996).
15. D. W. Fletcher-Holmes, and A. R. Harvey, "Spectral imaging with a hyperspectral fovea," J. Opt. A, Pure Appl. Opt. **7**(6), S298–S302 (2005).
16. M. R. Descour, C. E. Volin, E. L. Dereniak, K. J. Thome, A. B. Schumacher, D. W. Wilson, and P. D. Maker, "Demonstration of a high-speed nonscanning imaging spectrometer," Opt. Lett. **22**(16), 1271–1273 (1997).
17. W. R. Johnson, D. W. Wilson, W. Fink, M. Humayun, and G. Bearman, "Snapshot Hyperspectral Imaging in Ophthalmology," J. Biomed. Opt. **12**(1), 014036 (2007).
18. A. A. Wagadarikar, N. P. Pitsianis, X. Sun, and D. J. Brady, "Video rate spectral imaging using a coded aperture snapshot spectral imager," Opt. Express **17**(8), 6368–6388 (2009).

#123500 - $15.00 USD Received 28 Jan 2010; revised 11 Feb 2010; accepted 11 Feb 2010; published 3 Mar 2010

19. B. Lyot, "Filter monochromatique polarisant et ses applications en physique solaire," Ann. Astrophys. (Paris) **7**, 32 (1944).
20. G. Backus, and F. Gilbert, "The resolving power of gross Earth data," Geophys. J. Int. **16**(2), 169–205 (1968).
21. G. Muyo, I. Alabboud, A. Gorman, D. Mordant, I. McNaught, and A. R. Harvey, "Snapshot retinal oximetry", To be submitted to Optics Express (2010).
22. Jet Propulsion Laboratory, University of California, *http://speclib.jpl.nasa.gov/*

1. Introduction

Perhaps the most fundamental issue in the recording of spectral images is to devise and implement an efficient method for recording a three-dimensional spectral data cube using a two-dimensional detector array. The capture of a spectral data cube in a single snapshot is a particularly important challenge since it opens up the possibility of spectrally imaging time-varying phenomena. Traditional spectral imaging techniques involve time-sequential scanning of either a spatial or a spectral dimension combined with snapshot imaging of the other two dimensions [1], so that a spectral data cube is assembled over a period of time. These *modus operandi* are exemplified by a push-broom scan of a one-dimensional spectral imager across the required field of view [2], and the use of tunable spectral filtering [3] or imaging Fourier-transform spectrometry [4]. The application of these traditional time-sequential techniques is restricted to those situations where an extended recording time is acceptable, for example in microscopy [5], remote sensing [6, 7], and some examples of biomedical imaging [8]. In addition there is a significant signal-to-noise ratio penalty incurred by the reduced average optical throughput associated with spectral and spatial multiplexing [1]. Although the Fellget and Jacquinot advantages of Fourier-transform spectrometry offer high optical throughput, the noise degradation introduced during data inversion restricts the Fellget advantage to low-light imaging and the Jacquinot advantage is generally restricted to single-pixel, that is non-imaging, instruments [1].

There are many potential applications of spectral imaging for which snapshot or time-resolved operation and high optical sensitivity are essential; for example, for monitoring combustion dynamics [9, 10]; *in vivo* biomedical imaging where motion cannot be avoided, such as retinal imaging [11]; endoscopy [12]; and for surveillance [13]. Unfortunately snapshot spectral imaging techniques are notable by their scarcity, although clearly the conventional color camera is an example of low-resolution spectral imaging. Snapshot techniques that enable high spectral resolution include bulk-optic [14] or fiber-optic [15] reformatting of a two-dimensional image into a one-dimensional array, which forms the input of a conventional one-dimensional imaging spectrometer; the computed tomographic imaging spectrometer (CTIS), in which a diffractive optical element spectrally disperses the image at the detector and computer algorithms invert this data to recover a spectral data cube [16, 17]; and the use of image-plane spatio-spectral coding, which also requires inversion to enable image recovery [18]. We report here a new technique: the image-replicating imaging spectrometer (IRIS), which enables spectral demultiplexing of an image in a snapshot onto a single conventional detector array. Spectral filtering is achieved using cascaded two-beam polarizing interferometry within birefringent media, so optical efficiency is in principle 100% for a polarized input, whilst spatial-spectral demultiplexing using Wollaston-prism polarizing beam splitters allows for a very compact device. A spectral image is recorded directly without computation and without the noise amplification that can accompany inversion.

In the next section we describe the fundamental principles of IRIS, in section 3 we describe initial results, IRIS is compared to traditional spectral imaging techniques in section 4 and we conclude in section 5.

#123500 - $15.00 USD Received 28 Jan 2010; revised 11 Feb 2010; accepted 11 Feb 2010; published 3 Mar 2010

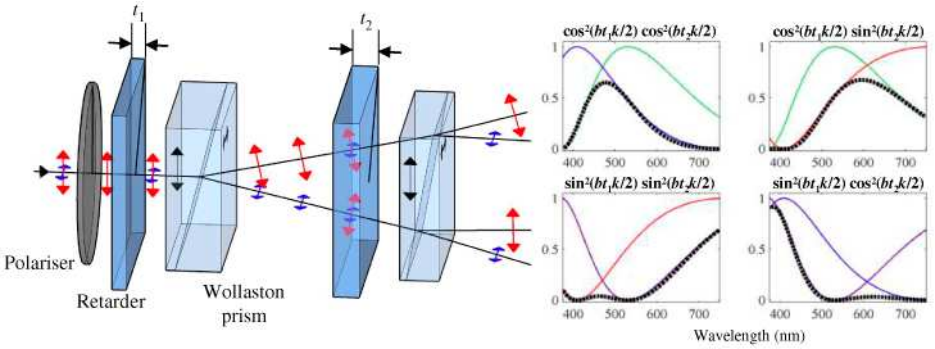

Fig. 1. Illustration of the demultiplexer splitting and filtering operation for an on-axis ray, for a four-channel system with the associated spectral transmission functions. The solid lines show the filter functions for each stage and the dashed lines in the dashed plots show the resultant, filter functions.

2. Principle of operation

The image-replicating imaging spectrometer (IRIS) employs a birefringent spectral demultiplexor (BSD) located in the pupil of a conventional imager. We will describe first the BSD and then explain its use within IRIS.

Light transmitted through the BSD is passed in sequence through a cascade of birefringent two-beam interferometers. The simplest example of a two-interferometer BSD is depicted in Fig. 1: the input birefringent interferometer consists of a wave plate sandwiched between an input polarizer and a Wollaston prism, where the fast axis of the wave plate is aligned at 45° to the optic axes of the polarizers. A light ray transmitted through this assembly is linearly polarized by the input polarizer and is subsequently resolved into two orthogonally polarized, co-linearly propagating, equal amplitude components by the wave plate birefringence. A path difference bt is introduced between these components, where b is the birefringence of the wave plate material and t is its thickness. Interference between these components occurs when they are resolved by the first Wollaston prism into two orthogonally polarized and divergent rays for which the spectral transmission functions

$$\tilde{\mathbf{T}} = \left[T_{\parallel}(k,t), T_{\perp}(k,t)\right] = \left[\cos^2 btk/2, \sin^2 btk/2\right] \qquad (1)$$

are consequentially applied to the components polarized parallel and perpendicular to the input polarizer respectively, where $k=2\pi/\lambda$ is the wavenumber. For clarity, the spectral dependence of b and the influence of non-normal transmission of the ray through the wave plate are omitted in this expression. The two divergent rays are transmitted through the second birefringent interferometer to yield four mutually divergent output rays to which four distinct spectral transmission functions are applied: one for each of the four distinct combinations of two spectral transmission functions of each of the two interferometers. Additional spectral filtering is achieved by additional birefringent interferometers so that an N-interferometer BSD consists of an input polarizer, followed by N wave plate-Wollaston-prism pairs. A single input ray is then spectrally demultiplexed into 2^N output rays after the Nth Wollaston prism where all possible factors of $\cos^2$ and $\sin^2$ interferometric filtering functions, as described by Eq. (1), are applied. When the BSD is placed in front of a conventional camera, filling its entrance pupil, the angular splitting introduced by the Wollaston prisms means that the output rays appear on a spatial matrix at the detector, Each ray can be indexed by the vector $\mathbf{p}=[p_1,p_2..p_N]$ where each p_i is an index of $\parallel$ or $\perp$ to indicate whether the associated ray after Wollaston prism i is polarized parallel or perpendicular to the ray transmitted through the preceding polarizer. The spectral transmission functions applied to the set of output rays, **p,** can then be written as

#123500 - $15.00 USD Received 28 Jan 2010; revised 11 Feb 2010; accepted 11 Feb 2010; published 3 Mar 2010

$$\tilde{T}_{\mathbf{p}}(k) = \prod_{i=1}^{N} T_{p_i}(k, t_i), \tag{2}$$

where t_i is the thickness of wave plate i. We describe here an example three-stage BSD for which the spectral transmission functions given by Eq. (2) are described by

$$\tilde{\mathbf{T}} = \begin{bmatrix} \tilde{T}_{\parallel,\parallel,\parallel}(k) \\ \tilde{T}_{\parallel,\parallel,\perp}(k) \\ \tilde{T}_{\parallel,\perp,\parallel}(k) \\ \tilde{T}_{\parallel,\perp,\perp}(k) \\ \tilde{T}_{\perp,\parallel,\parallel}(k) \\ \tilde{T}_{\perp,\parallel,\perp}(k) \\ \tilde{T}_{\perp,\perp,\parallel}(k) \\ \tilde{T}_{\perp,\perp,\perp}(k) \end{bmatrix} = \begin{bmatrix} \cos^2(b_1 t_1 k/2)\cos^2(b_2 t_2 k/2)\cos^2(b_3 t_3 k/2) \\ \cos^2(b_1 t_1 k/2)\cos^2(b_2 t_2 k/2)\sin^2(b_3 t_3 k/2) \\ \cos^2(b_1 t_1 k/2)\sin^2(b_2 t_2 k/2)\cos^2(b_3 t_3 k/2) \\ \cos^2(b_1 t_1 k/2)\sin^2(b_2 t_2 k/2)\sin^2(b_3 t_3 k/2) \\ \sin^2(b_1 t_1 k/2)\cos^2(b_2 t_2 k/2)\cos^2(b_3 t_3 k/2) \\ \sin^2(b_1 t_1 k/2)\cos^2(b_2 t_2 k/2)\sin^2(b_3 t_3 k/2) \\ \sin^2(b_1 t_1 k/2)\sin^2(b_2 t_2 k/2)\cos^2(b_3 t_3 k/2) \\ \sin^2(b_1 t_1 k/2)\sin^2(b_2 t_2 k/2)\sin^2(b_3 t_3 k/2) \end{bmatrix} \tag{3}$$

If all wave plate thicknesses are related by factors of two then $\tilde{\mathbf{T}}$ consists of eight distinct filter functions and $T_{\parallel,\parallel,\parallel}$ is identical to the filter function of the traditional Lyot filter [19] as used in the modern liquid crystal tunable filter. Optimization of the wave plate thicknesses (t_1, $t_2..t_N$) can yield a $\tilde{\mathbf{T}}$ that exhibits 2^N spectral filter functions with optimized filtering effectiveness. Useful figures of merit for defining optimum filter functions include minimum average side lobe level, maximum average orthogonality between bands, or a task-specific optimization for discriminating or measuring specific spectra. As can be appreciated from Eq. (3), each filter function exhibits a cyclic peak at approximate harmonics of a fundamental optical frequency (dispersion in the b_i causes the peaks to be not exactly harmonic). This is analogous to the free spectral range of a Fabry-Perot interferometer. A spectral band-pass filter is therefore required to define an overall spectral passband, for which all filter functions defined by $\tilde{\mathbf{T}}$ exhibit a single main lobe.

3. Experimental demonstration

We illustrate the IRIS principle using an eight-band system suitable for spectral imaging across the wavelength range 510-830nm. The calculated and measured values of $\tilde{\mathbf{T}}$ for the BSD using quartz wave plates of optimized thicknesses 0.12mm, 0.17m and 0.35mm are shown in Fig. 2(a). Measured spectral transmissions are recorded with the band-pass filter in place and are normalized with respect to a direct measurement of source spectrum. The black line shows the integral of the intensity of all bands and indicates an average optical efficiency of about 78% in polarized light. Attenuation of IRIS is dominated by the band-pass filter; transmission by the BSD is greater than 95% across the band. It can be observed that filter-function side lobe levels typically have peak values of 6% of the main transmission lobe, and for a grey spectrum the main transmission lobes contain an average of 85% of the energy. Optimization will generally yield band centers that are approximately equally spaced in optical frequency (rather than in optical wavelength), although depending on the cost-function used, some bands' centers may be close together, resulting in smaller spectral angles between these bands. It is possible, by suitable inversion, to transform the data to approximate a conventional spectrum with lower side lobes; for example, in Fig. 2(b) are shown the impulse response functions at the peak wavelengths following Backus-Gilbert inversion [20]. It should be noted that the spectral angles between transmission spectra are quite large on average (for the bands shown in Fig. 2(a), the average angle is 78^0 and the minimum spectral angle is 32^0), so a high-quality spectral image can also be recorded without inversion and, as is discussed in

#123500 - $15.00 USD Received 28 Jan 2010; revised 11 Feb 2010; accepted 11 Feb 2010; published 3 Mar 2010

section 4, the signal-to-noise ratio reduction accompanying inversion is generally just a few per cent lower than that of a hypothetical, fully-staring spectral imager.

The BSD is incorporated into the IRIS system shown in Fig. 3, which has been assembled using off-the-shelf compound lenses and integrated using a commercial cage-mount system. For this system, the field of view of 1.2° by 0.75° and an effective f-number of 6.4 required that the transverse width of the BSD wave plates and calcite Wollaston prisms have a minimum width of 20mm. An illustrative image of a linearly variable interference filter recorded with this IRIS is shown in Fig. 4(a). The filter was back-illuminated by diffuse, white light from a tungsten-halogen source. The plots superimposed on Fig. 4(a) are transverse intensity profiles taken across each image and correspond to the spectra of the BSD bands, as shown in Fig. 2(a), multiplied by the overall system spectral throughput. The unique capability of IRIS to record a two-dimensional multi-spectral movie without inversion is illustrated by Fig. 4(b), which shows an eight-band movie of a series of flame tests for the metal salts: Cu_2O (yellow-green flame), $CuSO_4$ (blue-green), Li_2SO_4 (red), Na_2CO_3 (yellow-orange) and $Na_2B_4O_7$ (yellow-green). As can be observed in the video sequence, the variation in the colors of the flame as the salts are sequentially introduced into the flame causes the expected relative brightnesses of the appropriate narrow-band image replications to vary. For example, in the still image in Fig. 4(b) for the introduction of $Na_2B_4O_7$, the flame is brightest in the two middle-right images corresponding to passbands centered on 571nm and 588nm in the yellow-green part of the spectrum.

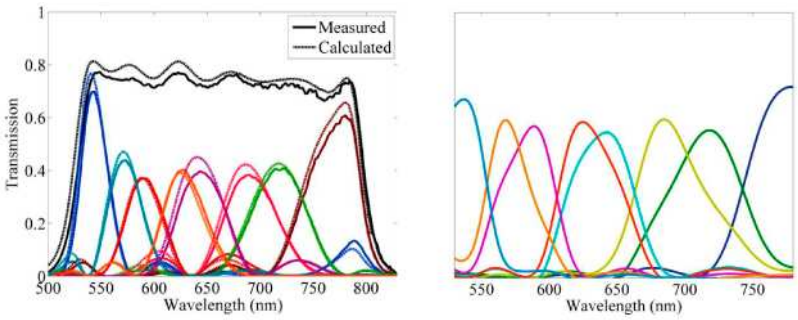

Fig. 2. (a) Calculated (dashed line) and measured optimized transmission bands for an eight-band BSD and (b) Impulse response at peak wavelengths following Backus-Gilbert inversion.

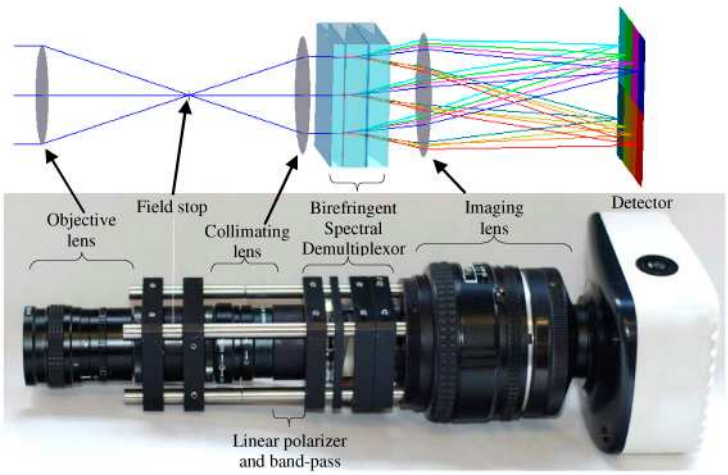

Fig. 3. (a) Diagram and (b) photograph of an eight-band image-replicating imaging spectrometer.

#123500 - $15.00 USD Received 28 Jan 2010; revised 11 Feb 2010; accepted 11 Feb 2010; published 3 Mar 2010

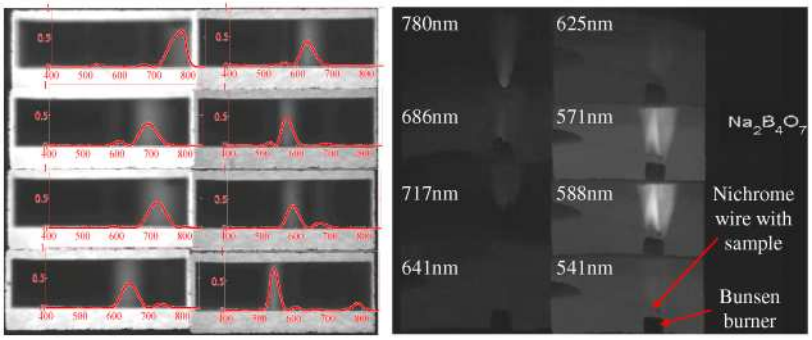

Fig. 4. (a) Images of a linearly variable interference filter recorded with the IRIS shown in Fig. 3(b) with superimposed intensity profiles. (b) A frame from a video sequence of a flame test for the chemicals: Cu_2O, $CuSO_4$, Li_2SO_4, Na_2CO_3 and $Na_2B_4O_7$., the peak wavelength for the each band is shown in the top left-hand corner of each sub-image (Media 1).

4. Discussion

Important parameters for IRIS include field of view (FoV), optical throughput and ability to distinguish component spectra. It is required that the splitting angle of the Wollaston prisms be sufficiently large to ensure separation of the spectral images on the detector array and this requires that the transverse width of the BSD increases with approximately the product of the FoV and the numerical aperture. Thus, although there is no fundamental limitation on the FoV or etendue of IRIS, beyond those common to all imaging systems, the high cost and lack of availability of such large Wollaston prisms mean that careful system optimization is necessary. As an example, a 16-band IRIS with f-5 optics and 28^0 FoV has been designed using 40mm wide calcite Wollaston prisms.

A more fundamental issue is the spectral dispersion in the splitting angle of the Wollaston prisms, since this causes the optical point spread function of the system to be spectrally dispersed at the detector array. In narrow-band systems, this dispersion for the full transmission spectrum is typically less than a pixel [21]. For broadband systems, such as the instrument described here, the PSF can be significantly dispersed, in the worst case across more than 10 pixels, and some mitigation is desirable. A mosaic of narrow-band filters located close to the detector can restrict transmission to that of the main spectral lobe so that the spectral smearing is reduced by a factor of $M=2^N$; that is, typically to about a pixel. Additional approaches using algorithmic inversion and achromatic Wollaston prisms are also under development.

While the presence of side lobes in Fig. 2(a) may be expected to degrade spectrometry performance, it is important to recall that the main goal of spectral imaging is normally to recover spectral abundances, **S**, rather than a pure spectrum. The image intensities at the detector array are $\mathbf{I} = \tilde{\mathbf{T}}.\mathbf{S}$ and hence inversion yields **S** directly without the need for an intermediate inversion step involving the use of improved transmission functions, such as those shown in Fig. 2(b). However, since the components of $\tilde{\mathbf{T}}$ are not quite orthogonal (in common with nearly all spectrometry systems), there is some reduction in the signal-to-noise ratio of **S** compared to **I**. A reduction in SNR occurs for all systems requiring inversion where the recorded spectral basis set is non-orthogonal; for example, in the case of a Fourier-transform spectrometer, the presence of the bias on the interferogram leads to a degradation in the SNR by a factor of $\sqrt{M}$ [1]. In the case of IRIS, for the recording of a typical set of smoothly varying spectra, such as those found in the ASTER data library [22], the resulting SNR is only 8% less than that of a hypothetical fully-staring, direct spectral imager, whereas the optical throughput is a factor of at least eight greater, so the SNR can be more than seven times greater than would be obtained in the same total recording time with an ideal time-sequential spectral imager.

#123500 - $15.00 USD Received 28 Jan 2010; revised 11 Feb 2010; accepted 11 Feb 2010; published 3 Mar 2010

5. Conclusion

The selection of an optimal spectral imaging technique depends very much on application requirements. IRIS is ideally suited to those applications requiring multi-spectral imaging with about 8 to 32 contiguous spectral bands where a snapshot capability is required. We believe IRIS is the first instrument to demonstrate multi-spectral imaging in eight (or more) bands without the need for computer inversion and image reconstruction. Additional important benefits of IRIS include the very high optical efficiency, the inherent robustness and compactness, and the highly efficient use of the available pixels in the detector array. The technique is usable at all wavelengths for which suitable birefringent materials exist: we have identified suitable materials for application at wavelengths between 0.2μm and 14μm. Applications where IRIS offers particular promise include real-time surveillance, remote sensing, and biomedical imaging.

Acknowledgments

This research was conducted with support from EPSRC and Selex-Galileo Avionics, Edinburgh.

#123500 - $15.00 USD Received 28 Jan 2010; revised 11 Feb 2010; accepted 11 Feb 2010; published 3 Mar 2010